Technical Note

Characterization of Interpolation Effects in Cine Anatomic and Phase-Velocity Images

John C. Wood, MD, PhD

Purpose: To compare actual and predicted frequency response of reconstruction algorithms applied to anatomic and phase-contrast velocity cine images.

Materials and Methods: Anatomic and phase-contrast velocity segmented cine gradient echo images were collected from a stationary, doped-agarose phantom, using non-phase-contrast cine and phase-contrast cine with one to three directional encodings, one to 16 views per segment, and nearest-neighbor or linear interpolation. Temporal power spectra from object pixels were fit to linear transfer function models; nearest-neighbor interpolation by a sinc function and linear interpolation by a sinc^2 function.

Results: Simple linear transfer function models predicted >98% of the observed power spectral variation. Finite word effects produced small systematic differences at high temporal frequency.

Conclusion: Temporal power spectra of cine images collected from stationary objects completely characterizes low pass filtration effects of interpolation.

Key Words: interpolation; frequency response; cine; phase-contrast; VPS; k-space; aliasing
J. Magn. Reson. Imaging 2003;18:266–271.
© 2003 Wiley-Liss, Inc.

ANATOMIC AND PHASE-CONTRAST velocity cine imaging are central to both adult and pediatric cardiovascular diagnosis (1–3). Prospectively gated cine acquisitions synchronize k-space sampling to the trigger signal; however flash artifacts from variable repetition time and incomplete cardiac cycle coverage limit their widespread use (4–7). Retrospective cine acquisitions eliminate these difficulties by using a constant repetition time over the entire cardiac cycle; the correct relationship between acquired phase and the cardiac cycle is restored during image reconstruction by temporal

interpolation for each view (5,6,8,9). Interpolation acts as a low pass filter, producing temporal blurring (8,10). For temporally interleaved, unsegmented cine phase-contrast images, the effective transfer function was demonstrated to be the following (10):

$$|H(f)| = (\text{sinc}^2(\pi N_v TRf)) \qquad (1)$$

where $|H(f)|$ is the transfer function magnitude, N_v is the number of velocity encodings, and *TR* is the repetition time. Linear interpolation was used, producing a sinc^2 transfer function (10). The number of velocity encodings is 2 for simple through-plane velocity measurements, and 4 for unbalanced, three-directional velocity estimates (10). Equation [1] demonstrates that the effective sampling period, given by the product of TR and the number of velocity encodings, determines the filter cutoff. This expression was validated over a wide range of repetition times, using a sinusoidal flow generator (10,11).

Non-segmented cine acquisitions require one heartbeat for each phase encode, producing long total acquisition times. Segmented k-space algorithms are typically used to reduce acquisition time (12,13). In this technique, consecutive TRs are grouped into segments which have a given number of views, reducing imaging time by the number of views-per-segment (VPS). Since the effective sampling period is increased by a factor of VPS, the corresponding interpolation filter cutoff is lowered by the same amount. Hence, Eq. [1] can be rewritten for segmented acquisitions as the following:

$$|H(f)| = (\text{sinc}^2(\pi m N_v TRf)) \qquad (2)$$

for linear interpolation, and as

$$|H(f)| = |\text{sinc}(\pi m N_v TRf)| \qquad (3)$$

for nearest-neighbor interpolation, where *m* represents the number of VPS (14). Sinusoidal flow generators have also been used to validate Eq. [2] and [3] for segmented cine phase-contrast velocity imaging.

Previous studies have two limitations, however. First, sinusoidal flow generators are expensive and not widely available (11). Secondly, anatomic sequences, such as steady-state free-precession cine imaging or spoiled steady-state gradient echo cine imaging cannot be eval-

uated in the same manner. Frequency response of anatomic sequences is important in cardiac imaging where cardiac motion may contribute significant high frequency power. Constructing realistic temporal frequency-response phantoms is not trivial; consequently, only numerical simulation had been previously applied to this problem (18). This paper demonstrates a much simpler and more general alternative technique to characterize interpolation effects in anatomic as well as phase-velocity cine sequences, using temporal spectra from images of a stationary, doped-agarose phantom.

THEORY

Any linear transfer function can be characterized completely by examining system output in response to a white noise input. Given an input, $x(t)$, consisting of complex white noise having variance, σ^2, a transfer function with impulse response, $h(t)$, and a measured output, $y(t)$, the following relationships hold:

$$y(t) = x(t) \otimes h(t) \tag{4}$$

$$Y(\omega) = X(\omega)H(\omega) \tag{5}$$

$$|Y(\omega)|^2 = |X(\omega)|^2|H(\omega)|^2 = \sigma^2|H(\omega)|^2 \tag{6}$$

where $\otimes$ represents the convolution operator. The output power, $|Y(\omega)|^2$, is simply the transfer function magnitude-squared scaled by the noise power.

For the current application, $h(t)$ is the temporal interpolation impulse response function. The input is the time-varying k-space representation, $I(k_x, k_y, t)$. For a stationary object, $I(k_x, k_y, t)$ contains a combination of temporally invariant object data, and temporally varying white Gaussian machine noise. The reconstruction process consists of temporal interpolation of $I(k_x, k_y, t)$ using the interpolation function $h(t)$, followed by Fourier transformation in two spatial dimensions to yield the time-varying image data. Although practical implementations are inherently discrete, continuous time and frequency representations are used here for simplicity of illustration. Using the continuous representation, reconstruction can be written as follows:

$$I_{\text{int}}(x, y, t) = \iint (I(k_x, k_y, t) \otimes h(t))e^{2\pi j(k_x x + k_y y)}dk_x dk_y \tag{7}$$

where $I(k_x, k_y, t)$ represents the unblurred, time-varying, k-space image and $I_{\text{int}}(x, y, t)$ is the interpolated, or blurred, time-varying, image representation (note that the terms blurred and unblurred represent temporal, not spatial, smoothing). Swapping the Fourier and convolution integrals yields the following:

$$I_{\text{int}}(x, y, t) = \iint (I(k_x, k_y, t)e^{2\pi j(k_x x + k_y y)}dk_x dk_y) \otimes h(t),$$
$$\tag{8}$$

$$= I(x, y, t) \otimes h(t), \tag{9}$$

where $I(x,y,t)$ represents the unblurred time-varying image. Fourier transformation with respect to t yields the following:

$$I_{\text{int}}(x, y, \omega) = I(x, y, \omega)H(\omega) \tag{10}$$

$$|I_{\text{int}}(x, y, \omega)|^2 = |I(x, y, \omega)|^2|H(\omega)|^2 \tag{11}$$

Although $I(x,y,\omega)$ is unblurred, it is not noiseless. For regions of the image where Rician noise effects can be ignored, i.e., (x,y) pairs with SNR >4, $I(x,y,\omega)$ can be written as a sum of the object and noise spectra (15),

$$|I(x, y, \omega)|^2 = |I_{\text{obj}}(x, y, \omega)|^2 + \sigma^2, \tag{12}$$

Equation [12] is true for all objects. However, if the object is stationary, temporal spectra represent delta functions at $\omega=0$ and Eq. [12] reduces to

$$|I(x, y, \omega)|^2 = \delta(\omega)|I_{\text{obj}}(x, y, \omega)|^2 + \sigma^2,$$
$$= |I_{\text{obj}}(x, y, 0)|^2 + \sigma^2, \tag{13}$$

and Eq. [11] can now be written as,

$$|I_{\text{int}}(x, y, \omega)|^2 = (|I_{\text{obj}}(x, y, 0)|^2 + \sigma^2)|H(\omega)|^2 \tag{14}$$

Therefore, the measured temporal power spectrum of a stationary object imaged with a retrospective cine sequence simply reflects the power spectrum of the interpolation function. The DC component of the power spectrum, $I_{\text{int}}(x,y,\omega = 0)$, contains information about the stationary object, but the higher temporal frequencies depend only upon the interpolation function and the noise power. Since $I_{\text{int}}(x,y,\omega = 0)$ is contaminated by object information, it must be estimated from the rest of the power spectrum: $I_{\text{int}}(x,y,|\omega| > 0)$. For clinically relevant choices of the sampling period (VPS*TR*Nv), Eq. [2] and [3] are relatively flat near the origin. In that case, $I_{\text{int}}(x,y,\omega=0)$ can be accurately approximated by its nearest neighbor. In a discrete Fourier transform representation of length N, the nearest neighbor is $I_{\text{int}}(x,y,\omega = \pm 2\pi/N[TR*VPS*Nv]))$. This approximation breaks down at long sampling periods (VPS*TR*Nv >80 msec), because the interpolating functions 2 and 3 become steep near the origin, leading to underestimation of $I_{\text{int}}(x,y,\omega = 0)$, i.e., $I_{\text{int}}(x,y,\omega = 0) - I_{\text{int}}(x,y,\omega = 2\pi/N[TR*VPS*Nv]) \gg 0$. A more sophisticated parametric model would be necessary to evaluate model accuracy at longer sampling periods. Comparison between measured and theoretical transfer functions was completed by normalizing both to unit power with calculation of mean-squared error between them.

MATERIALS AND METHODS

A 500-mL Nalgene bottle filled with 2% agar, 0.2% sodium azide, and 0.5-mM/liter gadopentate dimeglumine (Magnevist, Berlex Laboratories, Wayne, NJ) served as a stationary tissue phantom. Images were collected on a 1.5T CV$_i$ system (GE Medical Systems, Milwaukee, WI) using the head coil and CNV3 operating system. A custom-built TTL circuit provided a constant

simulated heart rate of 120 beats per minute. Most imaging parameters were matched for all three sequences with FOV 20 cm, thickness 8 mm, matrix 256×256, 1 NEX, and minimum-full TE. Segmented cine (FASTCINE, VASC-PC) had the following timing: 1) no velocity encoding: TR 9 msec, 112 reconstructed cardiac phases, VPS 1, 2, 4, 6, 8, 10, 12; 2) 1D velocity encoding: TR 8.4 msec, 64 reconstructed cardiac phases, VPS 1, 2, 4, 6, 8; and 3) 3D velocity encoding: VPS 1, 2, 4, 6, 32 reconstructed cardiac phases. Unsegmented cine (CINE) had TR of 21 msec for 3D velocity encoding and 18 msec otherwise. The maximum of 32 cardiac phases were reconstructed. Segmented balanced steady-state free-precession imaging (FIESTA) had a TR of 6.2 msec, 164 reconstructed cardiac phases, and 1, 2, 4, 6, 8, 12, 18, and 24 VPS.

Reconstruction could be toggled from linear interpolation (default) to nearest-neighbor using a single control variable. The manufacturer's algorithm for R-R interval correction produced no discernable spectral changes with the regular heart rates used in this study and was thus left in its default setting (17). Power spectra were calculated over a square region of interest wholly within a circular cross-section of the gel phantom magnitude images. Background noise is Rayleigh distributed and cannot be used to estimate the transfer function without deconvolution. Object SNR was approximately 40 to 1, ensuring a Gaussian noise distribution over the object (15). Measured spectra had DC-component nearest-neighbor correction, were normalized to unit power, and compared to Eq. [2] and [3], using custom MATLAB routines. Total sum of squared errors (SSE), representing noise power unexplained by the models, was calculated as a percentage of total power.

RESULTS

Figure 1 demonstrates the observed and predicted power spectral densities for nearest neighbor and linear interpolation of segmented cine SPGR images. The noise spectrum oscillates as predicted by sinc and sinc^2 functions. True zeros are not seen, with blunted minima. Observed spectra also have slightly greater high frequency power than predicted, particularly for low VPS, but overall agreement is excellent, particularly in the pass-band. Linear interpolation demonstrates lower side-band height and a sharper transition band; however, pass-band width is significantly narrower than for nearest-neighbor interpolation at comparable VPS. With the exception of VPS 2, the sum of SSE is 1% or less; the etiology of increased error for VPS 2 (SSE 3.5%) is unclear.

Curiously, at one VPS, spectra were indistinguishable from one another regardless of whether linear interpolation or nearest-neighbor interpolation was selected (not shown). Furthermore, observed spectra had significantly lower error from Eq. [3] than from Eq. [2], suggesting that nearest-neighbor interpolation is always used at 1 VPS. This was true for segmented cine SPGR N_v = 1, 2, and 4, but not the unsegmented cine SPGR implementation. Further support for this observation was obtained by examining the reconstructed
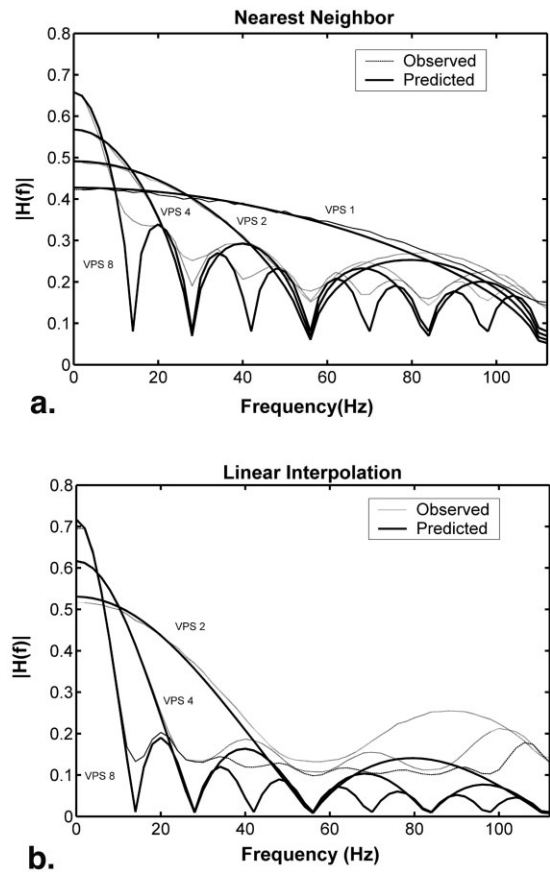

Figure 1. Magnitude of interpolation transfer function at 1, 2, 4, and 8 *VPS* is shown for nearest-neighbor (**a**) and linear (**b**) interpolation for segmented cine SPGR, *TR* 9 msec, N_v = 1. The bold line represents predicted intensity, the dashed line represents observed spectra; and both theoretical and observed data are normalized to unit power. Agreement is generally outstanding throughout the filter pass-band. Small deviations are observed in high frequency side lobes, particularly for linear interpolation.

images. Adjacent images were identical (i.e., images 1 and 2, 3 and 4, 5 and 6, etc.) for the VPS 1 case, regardless of whether linear or nearest-neighbor interpolation was requested. Such image pairing is expected for nearest-neighbor, but not linear, interpolation when reconstruction frequency (number of reconstructed phases/RR interval) is twice the acquisition frequency(1/(TR*VPS*Nv)). Since the interpolation is performed by proprietary reconstruction code prior to pass file creation, it is not possible to independently reconstruct from raw data. Manufacturer representatives familiar with the reconstruction code could not explain the discrepancy. This point demonstrates the utility of this simple method to interrogate the black-box of cine-reconstruction implementations.

The percent power deviation from the model is summarized in Table 1 for segmented SPGR, unsegmented SPGR, and segmented steady-state free-precession imaging. Overall agreement is excellent, with a median 98% power accounted for by Eq. [2] and [3].

The blunting of observed power spectra near the projected zeros may potentially represent quantization er-

Table 1
Percent Power Deviation for Segmented and Nonsegmented Cine SPGR

Technique	VPS	Nearest neighbor			Linear interpolation		
		$1N_v$	$2N_v$	$4N_v$	$1N_v$	$2N_v$	$4N_v$
Seg cine	1	.45	2.51	1.9	.54[a]	5.5[a]	1.7[a]
Seg cine	2	.57	1.48	2.01	3.51	3.93	4.11
Seg cine	4	1.11	1.38	4.19	1.17	2.52	3.65
Seg cine	6	1.13	2.88	10.8	.95	1.12	12.0
Seg cine	8	2.95	5.07	–	0.65	1.95	–
Seg cine	10	2.06	–	–	0.96	–	–
Seg cine	12	3.54	–	–	1.24	–	–
Seg bFFE	1	–	–	–	.25	.58	2.21
Seg bFFE	1	1.82	–	–	2.56[a]	–	–
Seg bFFE	2	0.77	–	–	3.32	–	–
Seg bFFE	4	0.83	–	–	1.19	–	–
Seg bFFE	8	1.19	–	–	0.45	–	–
Seg bFFE	12	2.44	–	–	0.47	–	–
Seg bFFE	18	2.44	–	–	1.17	–	–
Seg bFFE	24	4.89	–	–	3.12	–	–

[a]Data fit to Nearest-Neighbor Interpolation Model.

ror, as demonstrated in Figure 2. The bold line represents expected spectrum if floating point arithmetic were used exclusively; thin lines represent spectra from filtered noise, quantized to integers in the time domain, for different noise powers. As the noise power decreases relative to the unit integer, spectral flattening is observed with blunting of expected zeros and increased nonspecific high-frequency power. The observed

changes closely mimic deviations from ideal curves exhibited in Fig. 1, supporting the role of quantization.

Reconstruction aliasing represents another potential source of deviation of observed spectra from Eq. [2] and [3]. Reconstruction filters are not band-limited, having side lobes that will alias power down into the passband. Theoretically, aliased side-band power could account for zero-blunting. However, the degree of spectral oversampling, given by 2*VPS*Nv, did not appear to affect spectral blunting, suggesting that side-lobe aliasing was unimportant to this observation.

However, reconstruction undersampling profoundly affects observed spectra. The reconstruction filter passband lies between 0 and 1/(TR*VPS*Nv). Reconstruction aliasing will occur if the reconstruction frequency (number of phases/RR) is less than 2/(TR*VPS*Nv)(14). Figure 3 demonstrates anatomic segmented cine SPGR imaging using nearest-neighbor interpolation, 1 *VPS*, $N_v = 1$, *TR* 9 msec, heart rate 120 bpm (RR interval 0.5
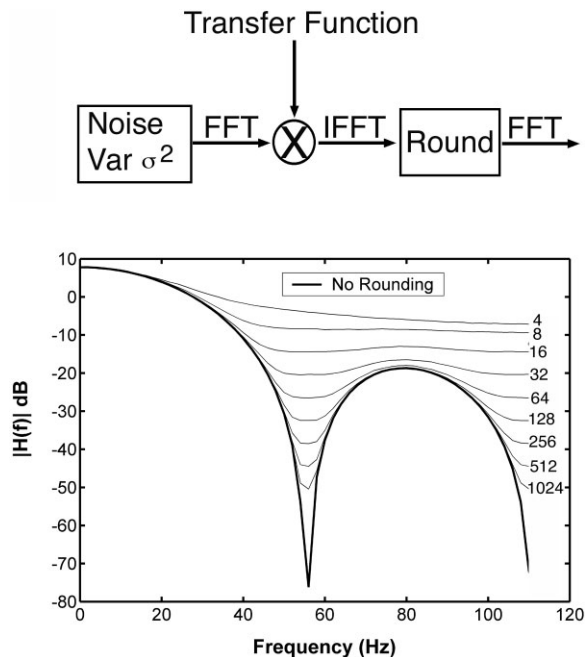

Figure 2. Effect of quantization on spectral shape. (Top) Flow chart diagramming synthesis method. White Gaussian noise was filtered in frequency space using Eq. [3] and floating point arithmetic. Rounding to nearest integer was performed in the time domain, followed by floating point power spectral calculation. (Bottom) Truncated nearest-neighbor transfer function magnitude spectra for VPS 2, as a function of noise power; spectra strongly resemble spectral blunting effects exhibited in Figs. 2, 3, and 4.
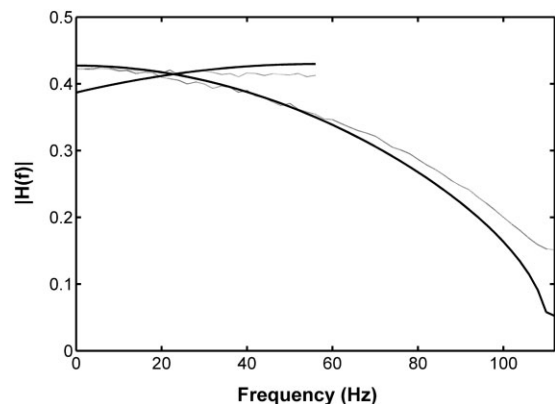

Figure 3. Demonstration of reconstruction aliasing for anatomic segmented cine SPGR imaging at one VPS. Bold line represents theoretical spectra, both aliased (line extending to 56 Hz) and unaliased (line extending to 112 Hz). Dashed lines represent observed spectra. The model accurately predicts the aliasing effects.

sec). The data sampling frequency is given by $1/(TR*Nv*VPS)$, or 112 Hz. When 112 phases are reconstructed (reconstruction frequency 224 Hz), a gentle frequency rolloff is observed as predicted by Eq. [3]. However when only 56 phases are reconstructed, aliasing completely flattens the observed spectrum. The degree of aliasing can be entirely predicted using Eq. [2] and [3] and discrete Fourier transform principles.

DISCUSSION

The purpose of this paper was to determine how well linear system theory describes low-pass filtering effects of cine-reconstruction algorithms for a wide range of clinical sequences. We used intrinsic machine noise to interrogate the effective transfer function of linear and nearest-neighbor interpolation. The overall agreement was excellent, with over 98% of the observed temporal power spectra accounted for by theory.

Two sources of error were identified. Systematic error was introduced at very long acquisition times from our sample-and-hold estimation of the transfer function DC component. A higher order fit would have reduced this effect, but our simple approximation was adequate for proof-of-concept. Secondly, temporal power spectra demonstrated blunting of the high-frequency rolloff as well as blunting of transfer function zero points. This phenomenon was closely mimicked through the use of integer arithmetic (Fig. 2). Truncation artifact introduces broadband noise having a power dependent on the image SNR. These effects, although interesting, were negligible.

The temporal power spectra can also be used to elucidate hidden reconstruction details. For example, we discovered that our segmented cine sequences always used nearest-neighbor interpolation when VPS was set to one, regardless of whether linear interpolation was requested in the sequence control variables. This difference could be significant if one were interrogating systems with high temporal-frequency content.

Cine reconstruction consists of interpolation from regularly or irregularly sampled views (16). An ideal interpolator is essentially a perfect low-pass filter having a cutoff at 1/sampling period (17). It corresponds to sinc interpolation in the time domain and can be approximated by Fourier zero-filling. Relative to the ideal response, both nearest-neighbor and linear interpolation have suboptimal frequency responses with narrower pass-bands, sloppy transition bands, as well as significant ringing. Figure 4 compares the frequency response of nearest-neighbor interpolator, linear interpolator, and ideal interpolator. Linear interpolation, the default technique on GE systems, has a -3-dB point which is only 31% of the ideal cutoff frequency. Nearest-neighbor interpolation has a -3-dB point that is 44% the width of the ideal interpolator, but less favorable side-lobe behavior. Feasibility of ideal interpolation has been demonstrated with k-space undersampling techniques, such as block regional interpolation scheme for k-space (BRISK), but have not been extensively studied (16). In addition to primary sinc interpolation, performed on the fly, post-interpolation inverse filtering in the temporal dimension is potentially feasible. That is,
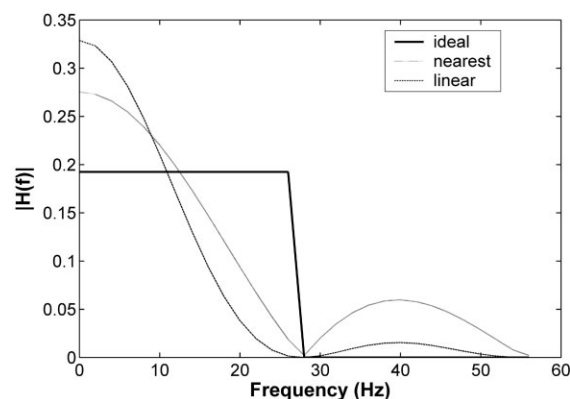

Figure 4. Comparision of ideal, nearest, and linear interpolation transfer functions, normalized to unit power, for VPS 4, *TR* 9 msec, $N_v = 1$. Half-power (-3dB) point is 0.32 of ideal for linear interpolation and 0.44 of ideal for nearest-neighbor.

if $H(\omega)$ represents the reconstruction transfer function and $I(\omega)$ the ideal interpolator response, a whitening filter, $G(\omega)$, could be designed such that $G(\omega)H(\omega) \approx I(\omega)$. Filter regularization would be needed near the zero point to prevent excessive noise amplification. Applying $G(\omega)$ to the observed data would approximate images produced by sinc interpolation. Potentially, improved temporal frequency response may allow comparable frequency response to present parameters, but in a shorter time period through the use of longer segments (larger VPS). Further work is needed to test these hypotheses.

In conclusion, cine-reconstruction details, such as type of interpolation, may not be well documented by the manufacturer. This paper demonstrates a simple technique to assess to the frequency characteristics of cine-reconstruction algorithms in a black-box fashion. Although a conceptually straightforward application of linear systems theory, it revealed unrecognized reconstruction details in our system. This study also extends the simple theoretical framework proposed by Polzin et al (14) to a wide range of imaging sequences and suggests potentially improved temporal response through post-processing.

REFERENCES

1. Fogel MA. Assessment of cardiac function by magnetic resonance imaging. Pediatr Cardiol 2000;21:59–69.
2. Beerbaum P, Korperich H, Barth P, Esdorn H, Gieseke J, Meyer H. Noninvasive quantification of left-to-right shunt in pediatric patients: phase-contrast cine magnetic resonance imaging compared with invasive oximetry. Circulation 2001;103:2476–2482.
3. Higgins CB, Byrd 3rd BF, Farmer DW, Osaki L, Silverman NH, Cheitlin MD. Magnetic resonance imaging in patients with congenital heart disease. Circulation 1984;70:851–860.
4. Lauzon ML, Holdsworth DW, Frayne R, Rutt BK. Effects of physiologic waveform variability in triggered MR imaging: theoretical analysis. J Magn Reson Imaging 1994;4:853–867.
5. Gatehouse PD, Firmin DN. The cardiovascular magnetic resonance machine: hardware and software requirements. Herz 2000;25:317–330.
6. Sondergaard L, Stahlberg F, Thomsen C, et al. Comparison between retrospective gating and ECG triggering in magnetic resonance velocity mapping. Magn Reson Imaging 1993;11:533–537.
7. Frayne R, Rutt BK. Frequency response of prospectively gated phase-contrast MR velocity measurements. J Magn Reson Imaging 1995;5:65–73.

8. Lenz GW, Haacke EM, White RD. Retrospective cardiac gating: a review of technical aspects and future directions. Magn Reson Imaging 1989;7:445–455.

9. Pelc NJ, Herfkens RJ, Shimakawa A, Enzmann DR. Phase contrast cine magnetic resonance imaging. Magn Reson Q 1991;7:229–254.

10. Frayne R, Rutt BK. Frequency response to retrospectively gated phase-contrast MR imaging: effect of interpolation. J Magn Reson Imaging 1993;3:907–917.

11. Frayne R, Holdsworth DW, Gowman LM, et al. Computer-controlled flow simulator for MR flow studies. J Magn Reson Imaging 1992;2:605–612.

12. Atkinson DJ, Edelman RR. Cineangiography of the heart in a single breath hold with a segmented turboFLASH sequence. Radiology 1991;178:357–360.

13. Edelman RR, Wallner B, Singer A, Atkinson DJ, Saini S. Segmented turboFLASH: method for breath-hold MR imaging of the liver with flexible contrast. Radiology 1990;177:515–521.

14. Polzin JA, Frayne R, Grist TM, Mistretta CA. Frequency response of multi-phase segmented k-space phase-contrast. Magn Reson Med 1996;35:755–762.

15. Gudbjartsson H, Patz S. The Rician distribution of noisy MRI data. Magn Reson Med 1995;34:910–914.

16. Doyle M, Walsh EG, Blackwell GG, Pohost GM. Block regional interpolation scheme for k-space (BRISK): a rapid cardiac imaging technique. Magn Reson Med 1995;33:163–170.

17. Oppenheim AV, Willsky AS, Nawab SH. Signals & systems. Upper Saddle River, NJ: Prentice Hall; 1997. 957 p.